

First discovery of an ultra-cool white dwarf benchmark in common proper motion with an M dwarf

M C Lam¹★, N C Hambly²†, N Lodieu^{3,4}, S Blouin⁵, E J Harvey¹, R J Smith¹, M C Gálvez-Ortiz⁶ and Z H Zhang⁷

¹*Astrophysics Research Institute, Liverpool John Moores University, IC2, LSP, 146 Brownlow Hill, Liverpool L3 5RF, UK*

²*Institute for Astronomy, University of Edinburgh, Royal Observatory of Edinburgh, Blackford Hill, Edinburgh EH9 3HJ, UK*

³*Instituto de Astrofísica de Canarias (IAC), Calle Vía Láctea s/n, E-38200 La Laguna, Tenerife, Spain*

⁴*Departamento de Astrofísica, Universidad de La Laguna (ULL), E-38206 La Laguna, Tenerife, Spain*

⁵*Los Alamos National Laboratory, P.O. Box 1663, Mail Stop P365, Los Alamos, NM 87545, USA*

⁶*Suffolk University, Madrid Campus, C/Valle de la Viña 3, 28003, Madrid, Spain*

⁷*School of Astronomy and Space Science, Key Laboratory of Ministry of Education, Nanjing University, Nanjing 210023, China*

Accepted 2020 February 25. Received 2020 January 15; in original form 2019 December 11

ABSTRACT

Ultra-cool white dwarfs are among the oldest stellar remnants in the Universe. Their efficient gravitational settling and low effective temperatures are responsible for the smooth spectra they exhibit. For that reason, it is not possible to derive their radial velocities or to find the chemistry of the progenitors. The best that can be done is to infer such properties from associated sources, which are coeval. The simplest form of such a system is a common proper motion pair where one star is an evolved degenerate and the other a main sequence star. In this work, we present the discovery of the first of such a system, the M dwarf LHS 6328 and the ultra-cool white dwarf PSO J1801+625, from the Pan-STARRS 1 3π survey and the *Gaia* Data Release 2. Follow-up spectra were collected covering a usable wavelength range of 3750 to 24500 Å. Their spectra show that the white dwarf has an effective temperature of 3550 K and surface gravity of $\log g = 7.45 \pm 0.13$ or $\log g = 7.49 \pm 0.13$ for a CO or He core, respectively, when compared against synthetic spectra of ultra-cool white dwarf atmosphere models. The system has slightly subsolar metallicity with $-0.25 < [\text{Fe}/\text{H}] < 0.0$, and a spatial velocity of $(U, V, W) = (-114.26 \pm 0.24, 222.94 \pm 0.60, 10.25 \pm 0.34) \text{ km s}^{-1}$, the first radial velocity and metallicity measurements of an ultra-cool white dwarf. This makes it the first and only benchmark of its kind to date.

Key words: binaries: visual – stars: low-mass – white dwarfs – solar neighbourhood.

1 INTRODUCTION

White dwarfs (WDs) are the final stage of stellar evolution of main sequence (MS) stars with zero age MS (ZAMS) mass less than $8M_{\odot}$. Since this mass range encompasses the vast majority of stars in the Galaxy, these degenerate remnants are the most common final product of stellar evolution, thus providing a good sample to study the history of stellar evolution and star formation in the Galaxy. In this state, there is little nuclear burning to replenish the energy they radiate away. As a consequence, the luminosity and temperature decrease monotonically with time. The electron degenerate nature means that a WD with a typical mass of $0.6M_{\odot}$ has

a similar size to the Earth, giving rise to their high densities, low luminosities, and large surface gravities. Typically, it takes less than $O(10^4)$ yr for metals to sink beneath the photosphere (Koester 2009), leaving only hydrogen and/or helium in the atmosphere. This leads to the lack of metallic features in the atmosphere. WDs with carbon and oxygen features are likely to have atypical evolutionary pathways (Kepler et al. 2016). The surface temperatures (T_{eff}) are $\sim 10^5$ K among the hottest WDs and can be as cool as ~ 3000 K at the faint end. When they cool below ~ 5000 K, the hydrogen and helium lines in the optical also disappear, leaving a featureless spectrum.

Ultra-cool white dwarfs (UCWDs) are the population of featureless cool WDs (spectral type DC) that exhibit collisionally induced absorption (CIA) features. This effect sets in at around $T_{\text{eff}} = 4000$ K. This temperature limit changes depending on the chemistry of the atmosphere. Recent works

★ E-mail: c.y.lam@ljmu.ac.uk

† E-mail: nch@roe.ac.uk

suggest a distinction between UCWD and IR faint cool WDs (Kilic et al. 2012; Gianninas et al. 2015). These cool and ultra-cool WDs have neutral colours and very low luminosities, so they are very hard to find and, therefore, study. Hence, they have been of interest to the science community for a number of years; however, we still know little about them. One of the keys is to better understand the structural and chemical evolution of the atmosphere as well as the core. Consequentially, they have significant impact in the understanding of the age and evolution of all Galactic components: through inversion of the colour-magnitude diagram (Vergely et al. 2002; Cignoni et al. 2006), or WD luminosity functions (Rowell 2013; Tremblay et al. 2014).

Common proper motion (CPM) binaries are gravitationally bound pairs formed when their birth cluster dissolves (Moeckel & Bate 2010; Moeckel & Clarke 2011; Kouwenhoven et al. 2011). Their wide physical separations mean that they have weak binding energy – the orbits can easily be disrupted; hence, they are assumed to be coeval and have evolved independently. A large sample of such binaries can be used to probe the Galactic gravitational potential (Chanamé & Gould 2004; Quinn & Smith 2009; Monroy-Rodríguez & Allen 2014; Correa-Otto et al. 2017). CPM systems containing a WD and a burning star provide the advantage that the age of the system can be estimated from WD cooling, while the progenitor chemistry and the radial velocity of the system can be extracted from the co-moving counterpart. Various works have studied their kinematics (Silvestri et al. 2001), contribution to the dark matter of the Galaxy (Silvestri et al. 2002), stellar chronology (Monteiro et al. 2006; Fouesneau et al. 2019), the initial-final mass relation (IFMR; Catalán et al. 2008; Zhao et al. 2012; Andrews et al. 2015; El-Badry et al. 2018). As the final products of post-asymptotic giant branch (AGB) stars, the mass distribution for WDs with companions is particularly useful to constrain wide binary orbital evolution as a function of spectral type (Silvestri et al. 2001).

In this work, we present the first glimpse of the UCWD PSO J180153.685+625419.450¹. It is the first UCWD found in CPM with a hydrogen-burning low-mass star where the chemistry of the progenitor system can be found. Section 2 describes the identification of this CPM pair and the follow-up observation programme is described in Section 3. The analyses of the M dwarf and the UCWD are presented in Section 4. At the end, in Section 5, we discuss the possible origin of the degenerate component.

2 IDENTIFICATION OF THE CPM PAIR

From the WD catalogue (Lam et al. 2019, hereafter L19) selected large proper motion sources from the Pan-STARRS 1 3 π Survey (Chambers et al. 2016; Magnier et al. 2016b,a,c; Waters et al. 2016), where there are a number of candidate UCWDs. When parallaxes from the *Gaia* DR2 (GDR2; *Gaia* Collaboration et al. 2016, 2018) became available,

¹ Due to its high proper motion, in Pan-STARRS DR1, this object is identified as two sources, the other source ID is PSO J180153.689+625419.758 with 19 epochs. The designation we have chosen, PSO J180153.685+625419.450, has 71 epochs of measurements.

PSO J1801+625 was immediately confirmed to have unusually low luminosity at $M_{\text{bol}} > 16$ mag. A proper motion and parallax cross match was performed and the WD was found to be in CPM with LHS 6328, a well catalogued M dwarf with a wealth of photometric information but never studied in detail given its unremarkable properties (see Fig. 1 for the false colour image from Pan-STARRS 1²). Further adding to the interest of this system is the tangential velocity from GDR2 (corresponding to the M dwarf distance) which suggests a likely thick disc origin, $v_{\text{tan}} = 4.74047 \times \mu \times D = 125.46 \text{ km s}^{-1}$. We list the parameters of the system in Table 1 and 2. Using photometry from Pan-STARRS 1, and the GDR2 parallax of the M dwarf, the best fit photometric effective temperature and atmospheric composition can be found by maximising the extended likelihood function from L19,

$$\mathcal{L} = -\frac{1}{2} \sum_i \left\{ \left[\frac{(\text{mag}_i - \text{DM}) - \text{model}_i}{\sigma_i} \right]^2 + \ln(2\pi\sigma_i^2) \right\} \quad (1)$$

where index i denotes the filter, mag is the observed magnitude, DM is the distance modulus, model is the synthetic photometry in absolute magnitude, and

$$\sigma_i^2 = \sigma_{\text{mag},i}^2 + \left[\frac{5 \log(e)}{\varpi} \right]^2 \sigma_{\varpi}^2 \quad (2)$$

is the combined uncertainty in magnitude $\sigma_{\text{mag},i}$ and in parallax σ_{ϖ} , where ϖ is the parallax.

For the low mass main sequence star the GDR2 Apsis-Priam effective temperature is 3675 K, placing it in the range where objects are consistently overestimated (Andrae et al. 2018). The mean offset is about 300 K, thus classifying this object as a M1-M3 dwarf (Rajpurohit et al. 2013, 2018). The angular separation of the system is 21.30'', combining with the distance of the M dwarf from Bailer-Jones et al. (2018), the projected physical separation of the system is 1554.1 AU, which is a common value for CPM wide binaries (Andrews et al. 2015; El-Badry et al. 2018).

This system was not reported by a recent large-scale CPM work using GDR2 data because of the large photometric uncertainty of the faint WD component (El-Badry et al. 2018). However, in our case, we have reliable photometry from Pan-STARRS 1 complemented with the high-quality astrometry from GDR2. With all of this supporting evidence we conducted a follow-up campaign described in the following Section.

3 FOLLOW-UP OBSERVATIONS

We collected additional photometric points and low resolution spectra with the 2 m Liverpool Telescope (LT; Steele et al. 2004), the 4 m William Herschel Telescope (WHT) and the 10 m Gran Telescopio Canarias, covering a wavelength range of 3750 – 25000 Å:

3.1 LT

Under the proposal JL18A03, low-resolution spectra of the UCWD and the M dwarf were collected with the SPRAT

² <https://pslimages.stsci.edu/cgi-bin/pslcutouts>

Parameter	LHS 6328	PSO J1801+625
^(a) R.A. (α)	18:01:54.228	18:01:53.691
^(a) Dec. (δ)	+62:53:59.432	+62:54:20.414
^(a) source_id	2159435171891858176	2159435274971074048
^(a) $\mu_\alpha / \text{mas yr}^{-1}$	10.210 ± 0.046	10.498 ± 1.122
^(a) $\mu_\delta / \text{mas yr}^{-1}$	362.712 ± 0.055	360.240 ± 0.964
^(a) ϖ / mas	13.6769 ± 0.0258	14.7551 ± 0.5680
^(a) ruwe	1.152	1.043
^(b) Distance / pc	$72.962^{+0.139}_{-0.138}$	$67.737^{+2.733}_{-2.532}$
^(c) G / mag	14.490 ± 0.0003	20.105 ± 0.007
^(c) G_{BP} / mag	15.632 ± 0.004	20.575 ± 0.081
^(c) G_{RP} / mag	13.430 ± 0.001	19.145 ± 0.053
^(d) B_{APASS} / mag	17.011 ± 0.011	—
^(d) V_{APASS} / mag	15.314 ± 0.062	—
^(e) g_{P1} / mag	16.016 ± 0.003	21.259 ± 0.028
^(e) r_{P1} / mag	14.769 ± 0.003	20.019 ± 0.018
^(e) i_{P1} / mag	13.875 ± 0.007	19.517 ± 0.024
^(e) z_{P1} / mag	13.419 ± 0.007	19.311 ± 0.035
^(e) y_{P1} / mag	13.181 ± 0.002	19.268 ± 0.027
^(f) J_{2MASS} / mag	12.031 ± 0.021	—
^(f) H_{2MASS} / mag	11.508 ± 0.022	—
^(f) K_{2MASS} / mag	11.292 ± 0.020	—
^(g) W_1 / mag	11.147 ± 0.023	—
^(g) W_2 / mag	10.979 ± 0.020	—
^(g) W_3 / mag	10.896 ± 0.051	—
^(g) W_4 / mag	> 9.380	—

Table 1. This table lists all the relevant archival data available in the public domain. All photometry is reported in AB magnitude except for the 2MASS magnitudes that are reported in the Vega system. ^(a) Positions are in equinox J2000.0 and epoch J2015.5 as reported in GDR2. ^(b) Distance taken from Bailer-Jones et al. (2018). ^(c) GDR2. ^(d) AAVSO Photometric All Sky Survey (APASS) (Henden et al. 2015). ^(e) Pan-STARRS 1 3 π Survey. ^(f) 2MASS (Skrutskie et al. 2006). ^(g) ALLWISE Data Release (Cutri et al. 2014).

Parameter	Value
DA Photometric ^(a) $T_{\text{eff}} / \text{K}$	3645^{+71}_{-56}
DA Photometric ^(a) Distance / pc	$58.8^{+1.6}_{-1.3}$
DA Bolometric Magnitude ^(a)	$16.25^{+0.07}_{-0.08}$
DB Photometric ^(a) $T_{\text{eff}} / \text{K}$	3158^{+25}_{-91}
DB Photometric ^(a) Distance / pc	$44.2^{+1.6}_{-2.0}$
DA Bolometric Magnitude ^(a)	$16.89^{+0.12}_{-0.10}$
Photometric ^(b) $T_{\text{eff}} / \text{K}$	4264^{+7}_{-6}
Photometric ^(b) $\log(\mathcal{M}_{\text{He}}/\mathcal{M}_{\text{H}})$	$-1.61^{+0.07}_{-0.05}$
DA Photometric ^(c) $T_{\text{eff}} / \text{K}$	3959
DA Photometric ^(c) $\log(g)$	8.045
DA Photometric ^(c) mass / \mathcal{M}_{\odot}	0.605
DB Photometric ^(c) $T_{\text{eff}} / \text{K}$	4121
DB Photometric ^(c) $\log(g)$	8.017
DB Photometric ^(c) mass / \mathcal{M}_{\odot}	0.578

Table 2. Derived properties (apart from the distance) of the UCWD. ^(a) Using Pan-STARRS 1 photometry fitting DA and DB models with fixed $\log(g) = 8.0$ as reported in L19. ^(b) Using Pan-STARRS 1 photometry and GDR2 parallax with fitting mixed atmosphere model with fixed $\log(g) = 8.0$. ^(c) Values reported by Gentile Fusillo et al. (2019) using GDR2 photometry and parallax.

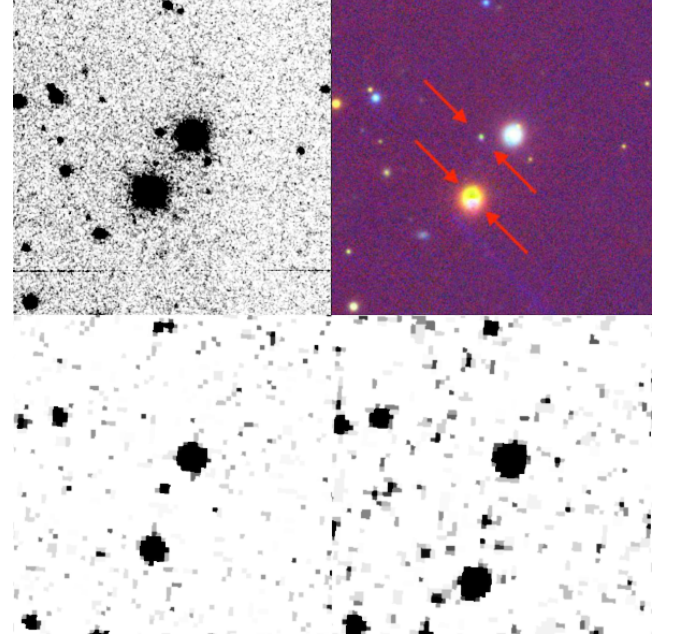


Figure 1. Clockwise from top left: LT/IO:O r -band image (2019); Pan-STARRS1 $g/i/y$ false-colour image (2012); the First Palomar Sky Survey plate image (1952); and Guide Star Catalogue 1 plate image (1983) of the PSO J1801+625 (faint object centred at the Pan-STARRS 1 image) and LHS 6328 (bright).

spectrograph in red-optimised mode (Piascik et al. 2014). For the UCWD, five 20-minute exposures were collected on each of the dark nights on 2018 August 6 and 7; for the M dwarf, five 2 min spectra were collected on 2018 August 10.

SPRAT has a resolving power of $R \sim 300$, covering a usable wavelength range of 4000 – 8000 Å (blue line in Fig. 3). We re-extracted the 1D spectra from the in-house calibrated 2D spectra (LSS_NONSS of the Level 2 products). Flux calibration was done using observations of the standard Hilt 102 taken on the same nights as the science observations. The spectra were then median-summed to give our final spectra, delivering a signal-to-noise ratio in the range 5 – 10 at different wavelengths for the UCWD and about 200 for the M dwarf. Some residual telluric features could not be completely removed.

In addition to the SPRAT spectra, three 20 min medium-resolution spectra were collected with FRODOSpec at the high resolution setting ($R \sim 5300$) covering a wavelength range of 5900 – 8000 Å. Due to the high sensitivity of the detector, we applied cosmic ray rejection with L.A.Cosmic (van Dokkum et al. 2012), before processing with the in-house automated pipeline (Barnsley et al. 2012).

The final spectrum is the weighted sum of the spectra from the 12 brightest fibres.

Additional photometric points were collected in Sloan g , r , i and z bands in the optical with IO:O and H band with IO:I in the near-infrared, which has a red cut-off at 17000 Å. The H -band data was slightly affected by the saturation residual mark from the neighbouring background star. All data were collected in photometric and dark condition.

3.2 WHT

Under the service proposal SW2018A35, two half-hour science frames were collected on each night during the 2018 August 1 and 2 under bright condition with a moon phase of around 70 per cent. The spectra were collected with WHT/ISIS using the R300B and R136R blue and red gratings centered at 4499 and 8651 Å, respectively. The Intermediate-dispersion Spectrograph and Imaging System (ISIS) is a high-efficiency double-arm spectrograph with a long-slit of up to 4 arcmin mounted on the WHT. The ISIS spectrograph is equipped with a blue and red detector made of 2048×4096 pixels whose sizes are 13.5 and 15 microns, respectively. The choice of this setup was made to maximize the wavelength coverage, i.e. where the LT/SPRAT and WHT/ACAM do not have coverage.

Standard long-slit single object data reduction was performed using IRAF (Tody 1986, 1993). 2D Spectra were median averaged separately for each night, before the two 1D spectra were optimally extracted. The final spectrum was the weighted average of the wavelength and flux calibrated spectra using the SPECTRES package³ (Carnall 2017). Standard observations of G93-48 were taken immediately before and after the observation on the respective nights, allowing for good removal of the telluric features, where only small residuals remain. The absolute flux calibration was done by comparing the integrated flux in the range of 4250 – 5250 Å between the absolute calibrated SPRAT spectrum and the ISIS blue arm. Both the red and blue ISIS spectra were then corrected by the same factor.

Three exposures of 600 s were obtained for the WD with the Auxiliary-port CAMera (ACAM) instrument mounted on the WHT on the night of 2019 July 29 between UT=21h37 and 22h10, under the program 095-WHT10/19A (PI Gálvez-Ortiz; observer Lodieu). One single exposure of 300 s was collected for the M dwarf companion starting at UT=21h27. ACAM offers low-resolution ($R \sim 400$) optical (3500 – 9400 Å) spectroscopy with a slit of 1 arcsec and the second-order blocking filter GG495. Arc lamps of Cu+Ne and tungsten flat field were collected immediately after at the position of the targets. A spectroscopic standard, Ross 640 (DZA5.5 Wesemael et al. 1993), was observed at the beginning of the night to correct for the response of the detector and calibrate the flux of our target.

The data were reduced using IRAF (Tody 1986, 1993). Bias subtraction and flat field correction were undertaken with the exposures obtained immediately following the science frames. The spectrum was extracted optimally choosing the aperture and the sky regions carefully. The final WHT/ACAM spectrum of the WD is displayed in green in

Fig. 3 while the spectrum of the M dwarf is shown in red in Fig. 2.

3.3 Gran Telescopio Canarias

Photometric and spectroscopic information was obtained with the Espectrografo Multiobjeto Infra-Rojo (EMIR Garzón et al. 2007, 2016) on the 10.4-m Gran Telescopio de Canarias (GTC) at the Observatorio del Roque de los Muchachos on the island of La Palma, under the programme GTC11-19A (PI: Lodieu). EMIR provides imaging and spectroscopic capabilities at near-infrared (0.9 – 2.5 microns) wavelengths. It is equipped with a 2048 × 2048 Teledyne HAWAII-2 HgCdTe detector with a pixel size of 0.2 arcsec per pixel, offering a 6.64 × 6.64 arcmin field-of-view.

Photometry was collected for the wide binary system on 2019 July 22 in service mode with a seeing of 0.6 arcsec, during bright time, and clear sky as part of programme GTC11_19A (PI Lodieu). Total exposure times of 175, 175, 315, and 1743 s were set for the Y , J , H , and K_s passbands with on-source individual integrations of 5 s and a pattern of seven dithers to avoid saturation of the brightest stars next to the common proper motion pair. Spectroscopy was conducted in service mode as part of the same GTC programme with a seeing of 0.7 arcsec, bright time, and clear skies. Four and eight on-source integrations of 360 s in an ABBA pattern were collected for the WD on 10 August 2019 with the YJ and HK grisms of EMIR covering the 0.899 – 1.331 and 1.454 – 2.428 micron intervals at a spectral resolution of about 500 with a slit width of 1.0 arcsec. A spectro-photometric standard star of spectral type B9III, HIP84021 (Hube 1970), was observed immediately after the target in both grisms.

The EMIR photometry and spectroscopy were reduced with the `pyemir` pipeline⁴. For the photometric data reduction, a median-filtered flat field was subtracted from each individual raw image before re-projecting the images with the `reproject` utility in Python. Afterwards, the images were astrometrically calibrated with Gaia sources present in the EMIR field of view. The parallactic angle was set for the photometric and spectroscopic observations. Ten stars in the field were used to compute the ensemble photometry. The H -band photometry agrees with the independent photometry from the LT. The photometric results are listed in Table 3 in the AB magnitude system.

For the spectroscopic data reduction, the `pyemir` pipeline implements a flat field correction, applies a wavelength calibration, and finds the offsets between the A and B positions of the spectra along the slit. The extraction of the spectra of the target and standard in each grism was conducted manually under IRAF, for selecting of the optimal apertures. The spectrum of the target was then divided by the spectrum of the standard and multiplied by a blackbody of the same temperature, smoothed to the EMIR resolution. The final spectra were down-sampled to 18.4 Å pix⁻¹, half the wavelength resolution of the optical spectra. The near-infrared spectrum of the WD is plotted in Figure 3.

³ <https://github.com/ACCarnall/spectres>

⁴ <https://pyemir.readthedocs.io/en/latest/>

Filter	Magnitude
g _{LT} /mag	21.12 ± 0.07
r _{LT} /mag	20.15 ± 0.04
i _{LT} /mag	19.51 ± 0.03
z _{LT} /mag	19.26 ± 0.03
J _{GTC} /mag	19.45 ± 0.02
H _{LT} /mag	19.90 ± 0.05
H _{GTC} /mag	19.96 ± 0.03
K _{GTC} /mag	20.40 ± 0.05

Table 3. Follow-up observations of the UCWD in AB magnitude.

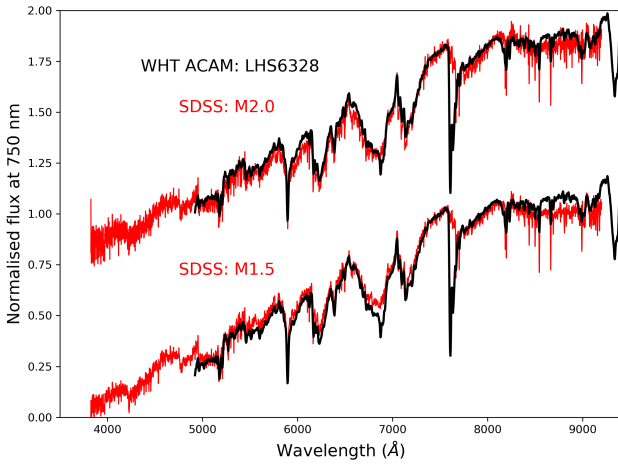


Figure 2. Template (red) fit of the ACAM spectrum (black) that gives the best-fit solution between type M1.5 and M2 with solar metallicity. Therefore, we assign it as a type $M1.75 \pm 0.25$ dwarf. The spectra are normalised at 7500 Å. The ACAM spectrum is not corrected for telluric absorption bands while the Sloan spectra (red) are; hence there is a clear discrepancy at around 7600 Å due to atmospheric O_2 .

4 ANALYSIS

4.1 LHS 6328

The ACAM spectrum of the MS star was compared against the low mass star template spectra from SDSS (Bochanski et al. 2007). Using the FRODOSpec spectra, we find that the metallicity indicators, $\zeta_{TiO/CaH}$, from Lépine et al. (2007) and Zhang et al. (2019) are 0.92 and 0.86, respectively. Both values suggest a slightly metal-poor M dwarf. The TiO5 spectral indexes show that they are dM1.70 (Reid et al. 1995), dM1.94 (Gizis 1997) and dM1.77 (Zhang et al. 2019), consistent with the best-fit solution by eye as a type $M1.75 \pm 0.25$ dwarf with roughly solar-metallicity (Fig. 2).

The radial velocity of the system was found with eight lines that can be identified by eye are measured from the median of the three FRODOSpec spectra, and compared against the BT-Settl⁵ model atmosphere of a M dwarf at 3500 K (Allard et al. 2012; Baraffe et al. 2015). The model spectrum is refraction-corrected with an air density of 0.733 amg based on the observing conditions. The me-

dian and standard deviation, computed from the product of 1.46 and the median absolute deviation (MAD), of the eight solutions are $v_r = -1.19 \pm 0.69 \text{ km s}^{-1}$. The full list can be found in the Appendix on Table A1. Using the `ASTROPY coordinates` and `time` packages, the barycentric correction was found to be -1.34 km s^{-1} yielding a barycentric radial velocity of $-2.53 \pm 0.69 \text{ km s}^{-1}$. By drawing 10000 samples from the Gaussian distributions of the proper motions, parallax and radial velocities with their associated uncertainties as the standard deviation, the `transform_to` method gives us the Galactic velocity⁶ $(U, V, W) = (-114.26 \pm 0.24, 222.94 \pm 0.60, 10.25 \pm 0.34) \text{ km s}^{-1}$, we use the default Solar spatial motion with the `AstroPy` package: $(U_\odot, V_\odot, W_\odot) = (11.1, 232.24, 7.25) \text{ km s}^{-1}$.

The absolute magnitudes of LHS 6328 in the near infrared are consistently $\sim 0.8 \text{ mag}$ fainter than the expected average value from the 8 pc sample from Table 3 of Lodieu et al. (2014). When compared with the average photometry from Pecaut & Mamajek (2013)⁷, this M dwarf is also consistently fainter in the optical by the same amount. However, it is worth noting that $\sim 0.9 \text{ mag}$ is within the 2 standard deviation of the sample used for averaging in Lodieu et al. (2014). This brightness also coincidentally puts it very close to the MS gap in the optical, discovered from the 100 pc sample from *Gaia* DR2 (Jao et al. 2018). See more discussion in Section 5.3.

4.2 PSO J1801+625

The final calibrated spectra of the UCWD are shown in Fig. 3. The usable spectral ranges are 3750 – 11000, 11500 – 13500, 14500 – 18000 and 19500 – 24000 Å. A black-body spectrum at 3808 K is plotted as a visual reference. The combined spectrum is smooth and does not show any absorption features, which could be the case for an extreme subdwarf. The only absorption features present were identified as coming from the residual sky lines, consistent with the spectrum expected from a WD with a cool atmosphere. Catalogued photometry from Pan-STARRS 1 g_{p1} , r_{p1} , i_{p1} and z_{p1} , GDR2 G , G_{BP} and G_{RP} and ensemble photometry with the field sources from the Liverpool Telescope g' , r' , i' , z' and H_{LT} , and from the GTC JEMIR, HEMIR & KEMIR photometry that were converted to flux values using the respective pivot wavelengths and overplotted onto the spectra. The photometric SED shows a remarkable resemblance to that of LSR J0745+2627 if placed at the same distance (Catalán et al. 2012a).

Model atmosphere analysis

We performed a fit to the available spectra of the UCWD to extract its atmospheric parameters. To do so we used the atmosphere models described in Blouin et al. (2018a,b). Different atmospheric compositions were tested (pure helium,

⁶ Detailed descriptions can be found at <https://docs.astropy.org/en/stable/api/astropy.coordinates.Galactocentric.html>

⁷ http://www.pas.rochester.edu/~emamajek/EEM_dwarf_UBVIJHK_colors_Teff.txt

⁵ <https://phoenix.ens-lyon.fr/Grids/BT-Settl>

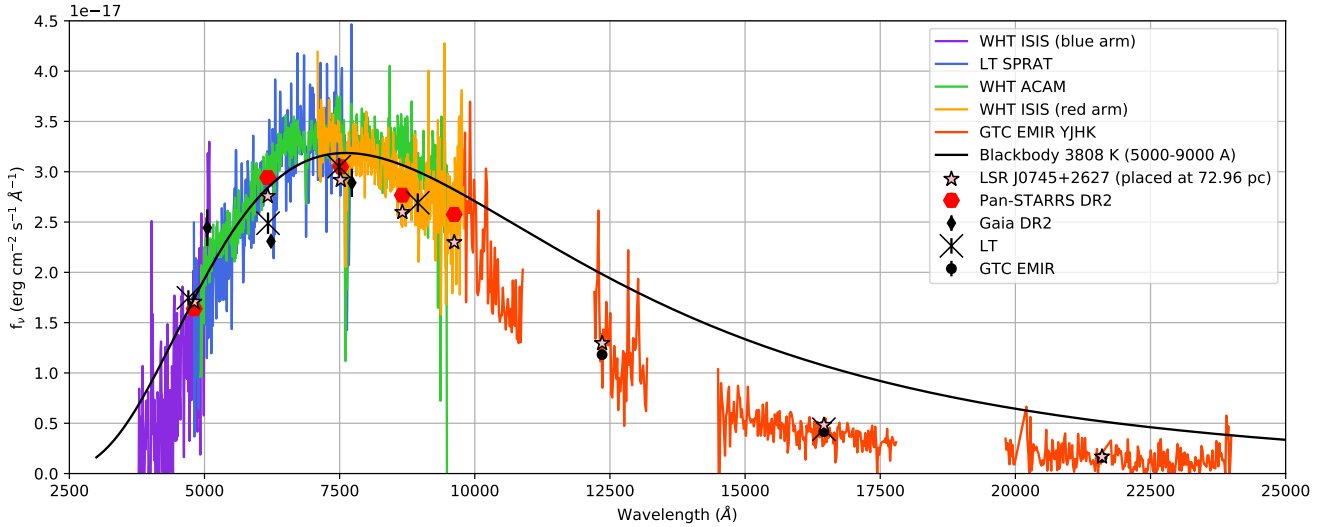


Figure 3. The spectra collected from WHT/ISIS blue and red arm (purple/orange), LT/SPRAT (blue), WHT/ACAM (green) and GTC/EMIR (red) overplotted with a black-body spectrum at 3808 K (black, χ^2 -fitted over the wavelength range of 5000 – 9000 Å). All optical spectra are re-sampled to 9.2 Å per pixel, while the EMIR spectra are smoothed to 18.4 Å per pixel. Only the usable ranges of the respective spectra are shown. The spectrum is smooth and does not show any absorption lines apart from the residual sky lines, consistent with the spectrum from a cool WD atmosphere. Pan-STARRS 1 *g/r/i/z/y* (left to right), *Gaia* DR2 *G_{BP}/G_{RP}* and LT/IO:O and IO:I *g/r/i/z/H* photometry (left to right) were converted to flux using the pivot wavelengths of the respective filters. All the overlapping ranges of the spectra agree well with each other.

pure hydrogen and mixed compositions with H/He abundance ratios ranging from 10^{-5} to 1) and we found that the best solution is by far a pure hydrogen model. Only a pure hydrogen model can successfully reproduce both the IR flux depletion due to H_2 – H_2 collision-induced absorption (CIA, Borysow et al. 2001) and the flux deficit at small wavelengths due to the far red wing of the Lyman α line broadened by collisions with H and H_2 (Kowalski & Saumon 2006). If helium is added to the model, the photospheric density becomes much higher, where H_2 –He CIA dominates (Blouin et al. 2017) and the model underestimates the IR flux.

The effective temperature and the solid angle were obtained by adjusting the model fluxes to the observed spectra using a Levenberg–Marquardt algorithm. As the distance D , 72.962 pc, is known from the *Gaia* parallax, the radius R can be computed from the solid angle $\pi R^2/D^2$. Then, thanks to evolutionary models, the radius and the effective temperature can be used to obtain the mass (and $\log g$) and the cooling time of the white dwarf. As the surface gravity resulting from this calculation was different from the one initially assumed to perform the fit, we repeated the procedure described above until the surface gravity converged.

Our best model achieves a good match to the whole spectral energy distribution (SED) of PSO J1801+625 as shown in Fig. 4. There seems, however, to be an offset between the model and the observations between 4000 and 6000 Å that appears to be due to an underestimation of the strength of the Lyman α broadening (see inset of Fig. 4). The atmospheric parameters of our best fit model are given in Table 4. Note that the effective temperature is similar to that of LSR J0745+2627 ($T_{\text{eff}} = 3880 \pm 90$ K, Catalán et al. 2012b), unsurprising given the similarity between the SEDs of both objects (see Fig. 3). In Table 4, we give the mass

	CO core	He core
T_{eff} (K)	3550 ± 150	
He/H	0	
R (R_{\odot})	0.0171 ± 0.0012	
M (M_{\odot})	0.30 ± 0.05	0.33 ± 0.06
$\log g$	7.45 ± 0.13	7.49 ± 0.13
τ_{cool} (Gyr)	5.1 ± 0.6	10.5 ± 1.5

Table 4. Atmospheric parameters of PSO J1801+625.

and cooling time corresponding to the case where the white dwarf has a CO core and to the case where it has a He core (which is more appropriate given the low mass found). For the CO core case we rely on the models of Fontaine et al. (2001) with $q(\text{He}) \equiv M_{\text{He}}/M_{\star} = 10^{-2}$ and a thick hydrogen envelope of $M_{\text{H}}/M_{\star} = 10^{-4}$. As for the He core case, we use the evolutionary tracks of Althaus et al. (2001)⁸, assuming once again $M_{\text{H}}/M_{\star} = 10^{-4}$.

5 DISCUSSION

To date, there are, including this work, 19 field UCWDs with their spectra confirmed. Their rarity and the lack of line features have made their investigation difficult at best. The lack of parallax measurements prior to *Gaia* DR2 and the inhomogeneity in the sample characteristics makes it difficult to do rigorous statistical analysis. Seven of the identified UCWDs were assumed to have a typical white dwarf surface gravity $\log g = 8.0$ (Kilic et al.

⁸ <http://fcaglp.fcaglp.unlp.edu.ar/~althaus/>

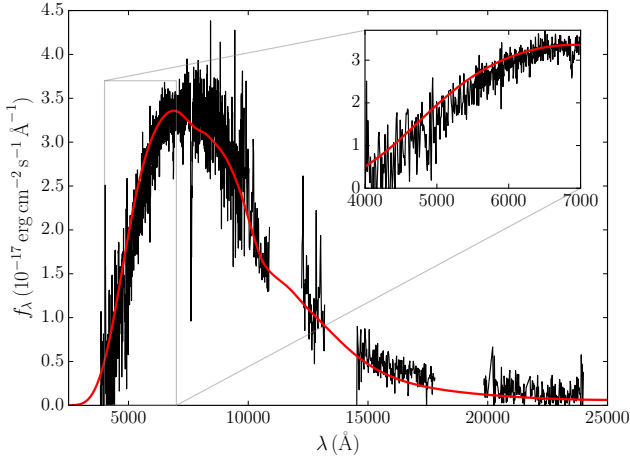


Figure 4. The best fit model of PSO J1801+625 indicates an effective temperature of 3550 K with low surface gravity. The best fit parameters are given in Table 4. The inset shows the small offset described in text.

2010; Holberg et al. 2016); while the remaining 11 had the gravity fitted as a free parameter: SSSJ1556-0806 (Rowell et al. 2008), J0146+1404, J1001+3903, J1238+3502, J1251+4403, J2239+0018A, J2242+0048, (Gianninas et al. 2015), LSH 3250 (Limoges et al. 2015), WD 0346+246 (Kilic et al. 2012), LHS 342, WD 0205-053 (Blouin et al. 2019)⁹. What is most surprising is how 9 of these 11 UCWDs have $\log g < 8.0$, the average mass of these being $0.36 M_{\odot}$. The least massive one, J2239+0018A, has $\log g = 6.95$, corresponding to a mass of $0.2 M_{\odot}$. For the two non-low mass UCWDs, WD 0346+246 and SSSJ1556-0806, both of them have their distances underestimated as compared to the Gaia distance from Bailer-Jones et al. (2018). Due to the degenerate dependency on the radius and distance of the object, when an object is fitted with a distance that is too small, the radius will also be too small. Hence, these two UCWDs, having $\log g = 8.3$ and 8.0 , respectively, are almost certainly going to be low-mass. Though, a thorough re-analysis is necessary to perform rigorous statistical analysis over the whole sample of UCWDs before drawing any conclusions.

We note that an over-density of low-mass WDs is expected at low effective temperatures as the result of the slowdown in their cooling due to latent heat release from the core crystallization and the extra thermal energy resulting from the first phase of convective coupling (see Fig. 15 of Bergeron et al. 2019). However, stellar evolution models show that it takes longer than the age of the Universe for an isolated star with $M < 0.45 M_{\odot}$ to turn into a WD. In this sense, the $0.36 M_{\odot}$ average mass for UCWDs is puzzling.

5.1 Low Mass Ultra-Cool White Dwarf

We have arrived with a few possibilities that can be attributed to the bulk of the low mass UCWDs in the known

sample: (1) higher mass ones do not exist; (2) unaccounted input physics in the current UCWD model, supported by the poor fits found in Gianninas et al. (2015); (3) they belong to a population of WD that evolved through a specific pathway.

End State of Single Metal-rich Star

There is evidence that an isolated metal-rich ($0.3 < [\text{Fe}/\text{H}] < 0.5$; Origlia et al. 2006; Gratton et al. 2006) star can lose sufficient mass to form a low mass WD (Hansen 2005; Kalirai et al. 2007; Kilic et al. 2007). In order to become an UCWD, they must have cooled for a few billion years regardless of the formation scenario. It would seem rather unlikely that the majority of the 11 low mass UCWDs have high metallicity. Furthermore, with the current picture of metal enrichment process of the Milky Way, it is unlikely to have this many old stars with enhanced metallicity in the early time of the Galaxy.

Common Envelope Evolution

The formation of a low-mass WD requires significant mass loss in the post-MS stage. The current understanding is that through common envelope (CE) evolution, the binary will produce a low mass WD; while in a stable Roche lobe overflow system, an extremely low mass WD would be produced instead (Li et al. 2019). Post-CE systems are tight binaries (hard), dynamically hard binaries become harder (separation decreases) when interacting with a third body (known as the Heggie’s Law, see Heggie 1975). If they were formed in binary systems, where is the missing companion star? Given the faintness of the UCWD, typically with $M_{\text{bol}} > 15$, any companions earlier than mid-T dwarf would have shown up in the optical and near-infrared images and/or spectra (see also the next scenario). It should be noted that given the low mass of a brown dwarf, if it should exist in the progenitor system, it could not have played a significant role in the late stage of the stellar evolution of the WD progenitor.

Unseen Companion(s)

Using the IRSA¹⁰ catalogue and time series tool, ZTF DR1 (Bellm et al. 2019a,b; Graham et al. 2019) with over 50 epochs in g and r bands, no variability is observed by either the UCWD or the M dwarf. Cross-correlations of the 3 up-sampled medium resolution spectra show shifts of 0.022 pixels between the first and second epoch and -0.004 pixels between the second and third epoch. This corresponds to 0.6 and -0.1 km s^{-1} respectively — with signal-to-noise ratios under 0.1, such that we disregard the values. Hence, it does not support a close, unresolved companion of any significant mass. The K_s band photometry reached ~ 21 mag. At $\sim 70 \text{ pc}$ a mid-T dwarf should be detectable (Faherty et al. 2012; Casewell et al. 2018), which can be in the form of IR excess if they are unresolved. Similarly, if they are resolved, they would be bright enough to show up in the W2 image at 70 pc (Tinney et al. 2014).

⁹ All the references here only refer to the most recently analysis that uses the most updated atmosphere models, most of them are not the original discovery articles.

¹⁰ <https://irsa.ipac.caltech.edu/>

Could they be the end products of low-mass X-ray binaries with a hidden neutron star in this system? Podsiadlowski et al. (2001) suggests that the end products are predominantly He and low-mass hybrid HeCO WDs. When the pulsar beam is not pointing towards us, there would not be any direct detection of the neutron star. Without absorption lines with which to measure radial velocity it is not possible to infer the presence of such a compact heavy object. Transits are not present in most binary systems, due to orbital inclination. In the stable Roche-lobe overflow or double helium core WD merger formation scenario of hot subdwarf B stars, the low-mass population cannot burn helium and they eventually evolve to become helium core WDs (Han et al. 2002, 2003). This tends to produce low mass WDs. In the case of both He and CO core WDs, this can be possible for symbiotic stellar evolution that happened at the early times of the Milky Way. HD 188112 is the prototype that bridges the late hot subdwarf B to a He core WD (Latour et al. 2016).

5.2 Typical Mass Ultra-Cool White Dwarfs

All empirical or theoretical initial-final mass relations (Catalán et al. 2008; Zhao et al. 2012; Andrews et al. 2015; El-Badry et al. 2018) tell the same story: *more massive stars leave behind more massive remnants*. UCWDs are old objects, they have been cooling for a few billion years. From the PARSEC stellar evolution model (Bressan et al. 2012), 1.5 and $2M_{\odot}$ solar-metallicity stars take ~ 3 and ~ 1.5 Gyr to become WDs, respectively. Their corresponding WD masses are $\sim 0.6M_{\odot}$, which would take ~ 10 Gyr for them to cool to 3500 K, assuming a pure hydrogen atmosphere. The combined age of 11 – 13 Gyr would be roughly that of the thick disc and the halo. For a $\sim 0.9M_{\odot}$ WD, which would have been a $\sim 5M_{\odot}$ MS star. Due to a smaller radius and low luminosity, it would take ~ 11 Gyr to reach 3500 K (see Fig. 12 of Bergeron et al. 2019, and note that $\sim 0.8M_{\odot}$ WD has the lowest cooling rate). More massive stars evolve quicker, so the total time required would be roughly the same as that required by WDs with typical masses.

A metal poor star evolves faster, so it is possible for a MS star slightly under $1.5M_{\odot}$ to become WDs, however, they also have lower total mass loss resulting in slightly more massive WDs that cool slower. Therefore, the total MS life time and WD cooling time for the metal poor systems is similar to those with solar metallicity.

The seven remaining spectroscopically confirmed UCWDs in the Montreal White Dwarf Database¹¹ do not have the surface gravity fitted as a free parameter, so it is unclear if any of those would fit into this category of UCWDs that we can treat them as singly evolved stars.

In order for PSO J1801+625 to be a typical mass WD, it has to be $\sim 45\%$ closer. This requires the parallax to be 10σ off for the UCWD and a few hundreds for the equidistant M dwarf. On the other hand, if the “low mass UCWD” is a pair of unresolved binary UCWDs, because of the degenerate nature of WD, the more massive it is, the smaller it becomes. At a given distance and temperature, their radii is a factor of $\sqrt{2}$ smaller in order for them to have the same

luminosity as a single low mass WD. This decrease would bring the mass of the WDs up to that of a typical WD. The total life time of the “unresolved binary CO-WDs” would be too long compared that expected for a CO-core WD. In any case, it does not seem probable to have all or most of the UCWDs mentioned in the previous section to be unresolved binaries with almost identical mass, radius, envelope composition and temperature.

5.3 What if all our measurements are outlying data points?

For a solar metallicity single M1.75 dwarf to have the apparent magnitude as we observed, it should be at ~ 110 pc. The discrepancy in the absolute magnitude of LHS 6328 and that from the averaged values of the solar neighbourhood sample is roughly 0.8 mag in all optical and near-infrared filters. NEOWISE (Wright et al. 2010; Mainzer et al. 2014) has over 1000 epochs in W1 & W2 bands, where they do not show sign of variability using the periodogram tool available on their webpage. Data from the Transiting Exoplanet Survey Satellite (TESS, Ricker et al. 2015; Swade et al. 2018) were period folded with Period04 (Lenz & Breger 2005) between 0 and 360 cycles/day in step of 0.000625 with no 5σ peaks detected above ~ 0.4 mmag¹². Hence, neither starspots nor occultation can be the explanation; any object that is big enough to remove 0.8 mag of light would have shown up in the spectra or photometry. If we consider any single observable to see how much it takes to compensate for the “lost flux”, it is not possible to explain the discrepancy without leading to contradicting spectral, photometric and astrometric information. In the following, we list the possibilities to explain, if our data gathering and template fittings have been unlucky throughout, and LHS 6328 is a mild outlier.

(i) In the *Gaia* DR2, LHS 6328 has an ASTROMETRIC_EXCESS_NOISE_SIG of 6.85, meaning its astrometric solution is unreliable. For the WD, it is close to the detection limit, so the parallax is also unreliable. If LHS 6328 is at the upper distance limit, 73.1 pc, it would lead to a dimming of 0.01 mag in the absolute magnitude.

(ii) The uncertainty in our M dwarf template fitting is 0.25 spectral type, while the absolute error can be as large as 0.5 spectral type, this can contribute a 0.1 mag of difference.

(iii) The metallicity indicator $\zeta_{\text{TiO}/\text{CaH}}$ indicates a slightly sub-solar metallicity, which puts LHS 6328 close to the border of dwarf and subdwarf. A typical subdwarf has a metallicity of $[\text{Fe}/\text{H}] = -0.5$; if LHS 6328 has $[\text{Fe}/\text{H}] = -0.25$, and combined with a shift in +0.25 spectral type (i.e. lower temperature), due to the reduced radiative pressure in the atmosphere. The radius becomes smaller by about 20% (Baraffe et al. 1997; Kesseli et al. 2019). This would correspond to a change of 0.2 mag.

(iv) In the case of SDSS filters, the dispersion in the magnitudes for a given spectral type is about 0.25 mag (West et al. 2005; Schmidt et al. 2010).

If LHS 6328 is 1.5σ from the average in all quantities, the total magnitude difference could reach 0.8 mag. This can account for the slightly spurious luminosity of a system

¹¹ <http://www.montrealwhitedwarfdatabase.org>

¹² TESS unique object ID: TIC 233068267

containing two single objects at ~ 70 pc, as supported by the Renormalised Unit Weight Error (RUWE, see Table 1) which are close to 1.

6 CONCLUSION

We have collected the spectra of an UCWD in common proper motion with a slightly metal poor M1.75 dwarf star, LHS 6328. The UCWD has an effective temperature of 3550 K, given its low mass at $0.33 M_{\odot}$, it is likely to have a He core, with a total cooling age of 10.5 ± 1.5 Gyr. This is most likely the remnant from a previously interacting binary that the companion is no where to be seen. This is the first system of a field UCWD with a pure hydrogen atmosphere that we can obtain the progenitor metallicity, $-0.25 < [\text{Fe}/\text{H}] < 0$, from its coeval main sequence companion. From the radial velocity measurement of the LHS 6328, we also have the first full 6D kinematics found for a UCWD, with $(U, V, W) = (-114.26 \pm 0.24, 222.94 \pm 0.60, 10.25 \pm 0.34) \text{ km s}^{-1}$, suggesting a thick disc-like velocity. Despite these measurement, the unclear origin of the low mass UCWD does not allow us to confidently draw any concrete conclusions. We propose a number of explanations but there is no evidence for any of the suggested scenarios. We believe it is necessary to run simulations on a wide range of configurations in order to understand what kind of evolution scenarios could have led to a system like LHS 6328 and PSO J1801+625.

ACKNOWLEDGEMENTS

ML acknowledges financial support from the OPTICON. ML thanks P. R. McWhirter for the frequency analysis on the M-dwarf variability.

NL was financially supported by the Spanish Ministry of Economy and Competitiveness (MINECO) under the grant AYA2015-69350-C3-2-P (2016-2019). NL thanks Lee Patrick, Alina Streblyanska, and the pyemir developers for their help during the reduction of the EMIR data.

SB acknowledges support from the Laboratory Directed Research and Development program of Los Alamos National Laboratory under project number 20190624PRD2.

The Liverpool Telescope is operated on the island of La Palma by Liverpool John Moores University in the Spanish Observatorio del Roque de los Muchachos of the Instituto de Astrofísica de Canarias with financial support from the UK Science and Technology Facilities Council.

The William Herschel Telescope and its service programme are operated on the island of La Palma by the Isaac Newton Group of Telescopes in the Spanish Observatorio del Roque de los Muchachos of the Instituto de Astrofísica de Canarias.

Based on observations made with the Gran Telescopio Canarias (GTC), installed in the Spanish Observatorio del Roque de los Muchachos of the Instituto de Astrofísica de Canarias, in the island of La Palma.

This work is partly based on data obtained with the instrument EMIR, built by a Consortium led by the Instituto de Astrofísica de Canarias. EMIR was funded by GRANTE-

CAN and the National Plan of Astronomy and Astrophysics of the Spanish Government.

This publication makes use of data products from the Two Micron All Sky Survey, which is a joint project of the University of Massachusetts and the Infrared Processing and Analysis Center/California Institute of Technology, funded by the National Aeronautics and Space Administration and the National Science Foundation.

This publication makes use of data products from the Wide-field Infrared Survey Explorer, which is a joint project of the University of California, Los Angeles, and the Jet Propulsion Laboratory/California Institute of Technology, funded by the National Aeronautics and Space Administration.

This paper includes data collected by the TESS mission. Funding for the TESS mission is provided by the NASA Explorer Program.

The Pan-STARRS1 Surveys (PS1) and the PS1 public science archive have been made possible through contributions by the Institute for Astronomy, the University of Hawaii, the Pan-STARRS Project Office, the Max-Planck Society and its participating institutes, the Max Planck Institute for Astronomy, Heidelberg and the Max Planck Institute for Extraterrestrial Physics, Garching, The Johns Hopkins University, Durham University, the University of Edinburgh, the Queen's University Belfast, the Harvard-Smithsonian Center for Astrophysics, the Las Cumbres Observatory Global Telescope Network Incorporated, the National Central University of Taiwan, the Space Telescope Science Institute, the National Aeronautics and Space Administration under Grant No. NNX08AR22G issued through the Planetary Science Division of the NASA Science Mission Directorate, the National Science Foundation Grant No. AST-1238877, the University of Maryland, Eotvos Lorand University (ELTE), the Los Alamos National Laboratory, and the Gordon and Betty Moore Foundation.

This work has made use of data from the European Space Agency (ESA) mission *Gaia* (<https://www.cosmos.esa.int/gaia>), processed by the *Gaia* Data Processing and Analysis Consortium (DPAC, <https://www.cosmos.esa.int/web/gaia/dpac/consortium>). Funding for the DPAC has been provided by national institutions, in particular the institutions participating in the *Gaia* Multilateral Agreement.

REFERENCES

- Allard F., Homeier D., Freytag B., 2012, *Philosophical Transactions of the Royal Society of London Series A*, 370, 2765
- Althaus L. G., Serenelli A. M., Benvenuto O. G., 2001, *MNRAS*, 323, 471
- Andrae R., et al., 2018, *A&A*, 616, A8
- Andrews J. J., Agüeros M. A., Gianninas A., Kilic M., Dhital S., Anderson S. F., 2015, *ApJ*, 815, 63
- Bailer-Jones C. A. L., Rybizki J., Fousneau M., Mantelet G., Andrae R., 2018, *AJ*, 156, 58
- Baraffe I., Chabrier G., Allard F., Hauschildt P. H., 1997, *A&A*, 327, 1054
- Baraffe I., Homeier D., Allard F., Chabrier G., 2015, *A&A*, 577, A42
- Barnsley R., Smith R., Steele I., 2012, in Ballester P., Egret D., Lorente N. P. F., eds, *Astronomical Society of the Pacific Con-*

- ference Series Vol. 461, Astronomical Data Analysis Software and Systems XXI. p. 517
- Bellm E. C., et al., 2019a, *PASP*, **131**, 018002
- Bellm E. C., et al., 2019b, *PASP*, **131**, 068003
- Bergeron P., Dufour P., Fontaine G., Coutu S., Blouin S., Genest-Beaulieu C., Bédard A., Rolland B., 2019, *ApJ*, **876**, 67
- Blouin S., Kowalski P. M., Dufour P., 2017, *ApJ*, **848**, 36
- Blouin S., Dufour P., Allard N. F., 2018a, *ApJ*, **863**, 184
- Blouin S., Dufour P., Allard N. F., Kilic M., 2018b, *ApJ*, **867**, 161
- Blouin S., Dufour P., Thibeault C., Allard N. F., 2019, *ApJ*, **878**, 63
- Bochanski J. J., West A. A., Hawley S. L., Covey K. R., 2007, *AJ*, **133**, 531
- Borysow A., Jorgensen U. G., Fu Y., 2001, *JQSRT*, **68**, 235
- Bressan A., Marigo P., Girardi L., Salasnich B., Dal Cero C., Rubele S., Nanni A., 2012, *MNRAS*, **427**, 127
- Carnall A. C., 2017, arXiv e-prints, p. arXiv:1705.05165
- Casewell S. L., Littlefair S. P., Parsons S. G., Marsh T. R., Fortney J. J., Marley M. S., 2018, *MNRAS*, **481**, 5216
- Catalán S., Isern J., García-Berro E., Ribas I., Allende Prieto C., Bonanos A. Z., 2008, *A&A*, **477**, 213
- Catalán S., et al., 2012a, *A&A*, **546**, L3
- Catalán S., et al., 2012b, *A&A*, **546**, L3
- Chambers K. C., et al., 2016, arXiv e-prints, p. arXiv:1612.05560
- Chanamé J., Gould A., 2004, *ApJ*, **601**, 289
- Cignoni M., Degl'Innocenti S., Prada Moroni P. G., Shore S. N., 2006, *A&A*, **459**, 783
- Correa-Otto J. A., Calandra M. F., Gil-Hutton R. A., 2017, *A&A*, **600**, A59
- Cutri R. M., et al., 2014, VizieR Online Data Catalog, p. II/328
- El-Badry K., Rix H.-W., Weisz D. R., 2018, *ApJ*, **860**, L17
- Faherty J. K., et al., 2012, *ApJ*, **752**, 56
- Fontaine G., Brassard P., Bergeron P., 2001, *PASP*, **113**, 409
- Fouesneau M., Rix H.-W., von Hippel T., Hogg D. W., Tian H., 2019, *ApJ*, **870**, 9
- Gaia Collaboration et al., 2016, *A&A*, **595**, A1
- Gaia Collaboration et al., 2018, *A&A*, **616**, A1
- Garzón F., et al., 2007, in Guzmán R., ed., Revista Mexicana de Astronomía y Astrofísica Conference Series Vol. 29, Revista Mexicana de Astronomía y Astrofísica Conference Series. pp 12–17
- Garzón F., et al., 2016, EMIR at the GTC: results on the commissioning at the telescope. p. 99081J, doi:10.1117/12.2232885
- Gentile Fusillo N. P., et al., 2019, *MNRAS*, **482**, 4570
- Gianninas A., Curd B., Thorstensen J. R., Kilic M., Bergeron P., Andrews J. J., Canton P., Agüeros M. A., 2015, *MNRAS*, **449**, 3966
- Gizis J. E., 1997, *AJ*, **113**, 806
- Graham M. J., et al., 2019, *PASP*, **131**, 078001
- Gratton R., Bragaglia A., Carretta E., Tosi M., 2006, *ApJ*, **642**, 462
- Han Z., Podsiadlowski P., Maxted P. F. L., Marsh T. R., Ivanova N., 2002, *MNRAS*, **336**, 449
- Han Z., Podsiadlowski P., Maxted P. F. L., Marsh T. R., 2003, *MNRAS*, **341**, 669
- Hansen B. M. S., 2005, *ApJ*, **635**, 522
- Heggie D. C., 1975, *MNRAS*, **173**, 729
- Henden A. A., Levine S., Terrell D., Welch D. L., 2015, in American Astronomical Society Meeting Abstracts #225. p. 336.16
- Holberg J. B., Oswalt T. D., Sion E. M., McCook G. P., 2016, *MNRAS*, **462**, 2295
- Hube D. P., 1970, Mem. RAS, **72**, 233
- Jao W.-C., Henry T. J., Gies D. R., Hambly N. C., 2018, *ApJ*, **861**, L11
- Kalirai J. S., Bergeron P., Hansen B. M. S., Kelson D. D., Reitzel D. B., Rich R. M., Richer H. B., 2007, *ApJ*, **671**, 748
- Kepler S. O., Koester D., Ouyang G., 2016, *Science*, **352**, 67
- Kesseli A. Y., et al., 2019, *AJ*, **157**, 63
- Kilic M., Stanek K. Z., Pinsonneault M. H., 2007, *ApJ*, **671**, 761
- Kilic M., et al., 2010, *ApJS*, **190**, 77
- Kilic M., Thorstensen J. R., Kowalski P. M., Andrews J., 2012, *MNRAS*, **423**, L132
- Koester D., 2009, *A&A*, **498**, 517
- Kouwenhoven M. B. N., Goodwin S. P., Davies M. B., Parker R. J., Kroupa P., Malmberg D., 2011, in Qain S., Leung K., Zhu L., Kwok S., eds, Astronomical Society of the Pacific Conference Series Vol. 451, 9th Pacific Rim Conference on Stellar Astrophysics. p. 9 (arXiv:1108.4505)
- Kowalski P. M., Saumon D., 2006, *ApJL*, **651**, L137
- Lam M. C., et al., 2019, *MNRAS*, **482**, 715
- Latour M., et al., 2016, *A&A*, **585**, A115
- Lenz P., Breger M., 2005, *Communications in Asteroseismology*, **146**, 53
- Lépine S., Rich R. M., Shara M. M., 2007, *ApJ*, **669**, 1235
- Li Z., Chen X., Chen H.-L., Han Z., 2019, *ApJ*, **871**, 148
- Limoges M. M., Bergeron P., Lépine S., 2015, *ApJS*, **219**, 19
- Lodieu N., Pérez-Garrido A., Béjar V. J. S., Gauza B., Ruiz M. T., Rebolo R., Pinfield D. J., Martín E. L., 2014, *A&A*, **569**, A120
- Magnier E. A., et al., 2016a, arXiv e-prints, p. arXiv:1612.05240
- Magnier E. A., et al., 2016b, arXiv e-prints, p. arXiv:1612.05242
- Magnier E. A., et al., 2016c, arXiv e-prints, p. arXiv:1612.05244
- Mainzer A. K., et al., 2014, in American Astronomical Society Meeting Abstracts #223. p. 217.08
- Moeckel N., Bate M. R., 2010, *MNRAS*, **404**, 721
- Moeckel N., Clarke C. J., 2011, *MNRAS*, **415**, 1179
- Monroy-Rodríguez M. A., Allen C., 2014, *ApJ*, **790**, 159
- Monteiro H., Jao W.-C., Henry T., Subasavage J., Beaulieu T., 2006, *ApJ*, **638**, 446
- Origlia L., Valenti E., Rich R. M., Ferraro F. R., 2006, *ApJ*, **646**, 499
- Pecaut M. J., Mamajek E. E., 2013, *ApJS*, **208**, 9
- Piasek A. S., Steele I. A., Bates S. D., Mottram C. J., Smith R. J., Barnsley R. M., Bolton B., 2014, in Ground-based and Airborne Instrumentation for Astronomy V. p. 91478H, doi:10.1117/12.2055117
- Podsiadlowski P., Rappaport S., Pfahl E., 2001, in Vanbeveren D., ed., Astrophysics and Space Science Library Vol. 264, The Influence of Binaries on Stellar Population Studies. p. 355 (arXiv:astro-ph/0109386), doi:10.1007/978-94-015-9723-4_26
- Quinn D. P., Smith M. C., 2009, *MNRAS*, **400**, 2128
- Rajpurohit A. S., Reylé C., Allard F., Homeier D., Schultheis M., Bessell M. S., Robin A. C., 2013, *A&A*, **556**, A15
- Rajpurohit A. S., Allard F., Teixeira G. D. C., Homeier D., Rajpurohit S., Mousis O., 2018, *A&A*, **610**, A19
- Reid I. N., Hawley S. L., Gizis J. E., 1995, *AJ*, **110**, 1838
- Ricker G. R., et al., 2015, *Journal of Astronomical Telescopes, Instruments, and Systems*, **1**, 014003
- Rowell N., 2013, *MNRAS*, **434**, 1549
- Rowell N. R., Kilic M., Hambly N. C., 2008, *MNRAS*, **385**, L23
- Schmidt S. J., West A. A., Hawley S. L., Pineda J. S., 2010, *AJ*, **139**, 1808
- Silvestri N. M., Oswalt T. D., Wood M. A., Smith J. A., Reid I. N., Sion E. M., 2001, *AJ*, **121**, 503
- Silvestri N. M., Oswalt T. D., Hawley S. L., 2002, *AJ*, **124**, 1118
- Skrutskie M. F., et al., 2006, *AJ*, **131**, 1163
- Steele I. A., et al., 2004, in Oschmann Jacobus M. J., ed., Society of Photo-Optical Instrumentation Engineers (SPIE) Conference Series Vol. 5489, Ground-based Telescopes. pp 679–692, doi:10.1117/12.551456
- Swade D., Fleming S., Jenkins J. M., Latham D. W., Morgan E., Mullally S. E., Sparks W., Vanderspek R., 2018, in Proc. SPIE. p. 1070415, doi:10.1117/12.2312066
- Tinney C. G., Faherty J. K., Kirkpatrick J. D., Cushing M., Morley C. V., Wright E. L., 2014, *ApJ*, **796**, 39

BT-SETTL / Å	Measured / Å	Radial Velocity / km s ⁻¹
6122.68	6122.5	-0.88
6162.63	6162.5	-0.63
6450.30	6449.9	-1.86
6463.06	6463.0	-0.28
7326.70	7326.4	-1.23
7511.59	7511.3	-1.16
7665.50	7665.1	-1.57
7699.56	7699.0	-2.18

Table A1. The wavelengths of the model absorption lines from BT-SETTL are corrected with an air density of 0.733 amg based on the observing conditions. The 8 lines that can be identified by eyes are used to compute the radial velocities.

- Tody D., 1986, The IRAF Data Reduction and Analysis System. p. 733, [doi:10.1117/12.968154](https://doi.org/10.1117/12.968154)
- Tody D., 1993, IRAF in the Nineties. p. 173
- Tremblay P. E., Kalirai J. S., Soderblom D. R., Cignoni M., Cummings J., 2014, [ApJ](#), **791**, 92
- Vergely J. L., Köppen J., Egret D., Bienaymé O., 2002, [A&A](#), **390**, 917
- Waters C. Z., et al., 2016, arXiv e-prints, [p. arXiv:1612.05245](#)
- Wesemael F., Greenstein J. L., Liebert J., Lamontagne R., Fontaine G., Bergeron P., Glaspey J. W., 1993, [PASP](#), **105**, 761
- West A. A., Walkowicz L. M., Hawley S. L., 2005, [PASP](#), **117**, 706
- Wright E. L., et al., 2010, [AJ](#), **140**, 1868
- Zhang S., et al., 2019, [ApJS](#), **240**, 31
- Zhao J. K., Oswalt T. D., Willson L. A., Wang Q., Zhao G., 2012, [ApJ](#), **746**, 144
- van Dokkum P. G., Bloom J., Tewes M., 2012, L.A.Cosmic: Laplacian Cosmic Ray Identification (ascl:1207.005)

APPENDIX A: APPENDIX

The 8 lines used for computing the radial velocity of the M dwarf are listed in Table A1. The spectrum used for the measurement is the median of the three 20-minutes FRODOSpec spectra.